Jet pressure-spectra estimation from single-snapshot tomographic PIV

González, G.; Ragni, Daniele; Avallone, Francesco; Schneiders, Jan; Casalino, Damiano; Ianiro, Andrea

DOI
10.2514/6.2018-3293

Publication date
2018

Document Version
Final published version

Published in
2018 AIAA/CEAS Aeroacoustics Conference

AIAA AVIATION Forum
June 25-29, 2018, Atlanta, Georgia
2018 AIAA/CEAS Aeroacoustics Conference

10.2514/6.2018-3293

Jet Pressure-Spectra Estimation from Single-Snapshot Tomographic PIV

G. González* , D. Ragni† , F. Avallone‡ , J. Schneiders§ , D. Casalino¶
Delft University of Technology, Kluyverweg 1, 2629HS, Delft, The Netherlands

and A. Ianiro‖
Universidad Carlos III de Madrid, Avenida de la Universidad 30, 28911 Leganés, Madrid, Spain

The analysis of the unsteady flow field of an axisymmetric subsonic jet at Reynolds numbers between 5,000 and 20,000 and computation of its unsteady pressure field is carried out from single snapshots of tomographic PIV measurements (acquisition rate 0.8 Hz). This is achieved by a recently developed pressure-evaluation technique based upon the vortex-in-cell (VIC) methodology. The technique allows for a finite time-marching of the instantaneous 3D velocity fields obtained from low-repetition PIV systems. A time series of velocity fields in 3D is obtained, which is integrated into unsteady pressure by use of the Navier-Stokes momentum equation. Despite the limitations in the finite-time marching of the measured structures due to the size of the acquired tomographic volume, spectra of pressure fluctuations can be extracted in a frequency range between 800Hz and 20kHz. Fair agreement was found between the experimentally computed pressure spectra and the respective values found in literature. Further work is dedicated to exploit the full potential of the technique by attempting a sound pressure level integration of the noise sources from the unsteady fields.

I. Introduction

Turbulent jets are among the most investigated flows in relation to several engineering applications, for both aerodynamic and aeroacoustic complexity [1]. In particular, the mixing of the flow features at the exit of the nozzle is cause of many interesting phenomena, which are difficult to be predicted. Amongst many, axis-switching is one of the most interesting, as it is associated with an earlier transition to turbulent regime and with the change of the flow topology along the jet development. The jet mixing with the surrounding ambient air and the axis-switching are additionally highly dependent on the exit Reynolds-number of the jet, which ,in turn, depends on its density and temperature. Consequently, the aeroacoustic modes associated with the interaction of coherent structures such as pairing events and break-down or dissipation of the flow structures are the result of the jet development from the near field to the far one.

The simultaneous presence of large scale coherent structures and small turbulent eddies makes it particularly difficult to link the measured aerodynamic flow modes with the acoustic ones [2]. Either in the low or high-speed regime, many experimental studies have been recently directed to the refinement of aeroacoustic models for the prediction of jet-mixing noise or to explain Mach number, temperature and frequency dependence of the sound produced. One of the most interesting findings is that large coherent structures significantly populate both low and high speed jets, contributing to the radiation of the sound toward downstream directions especially at relatively high Mach numbers [3][4]. Due to their heavy unsteadiness and multidimensionality, these interacting structures are substantially difficult to be accurately measured, already at low speed.

While previous models [5] [6] in fact, were assuming that given azimuthal components of the aerodynamic source were related to the same azimuthal mode in the sound field, recent experimental investigations suggested that the near field turbulent jet flow has already large scale wavy patterns. These patterns have been additionally found in the pressure correlations measured between probes separated by considerably more than the local integral length-scale [2]. Already for a single jet configuration, the mechanism of sound generation at angles upstream of the peak is still unknown, with

*Master Student, AWEP Department, ggonzalezsaiz@tudelft.nl, AIAA member.
†Assistant Professor, AWEP Department, d.ragni@tudelft.nl, AIAA member.
‡Assistant Professor, AWEP Department, f.avallone@tudelft.nl, AIAA member.
§PhD Candidate, AWEP Department, J.F.G.Schneiders@tudelft.nl, AIAA member.
¶Full Professor, AWEP Department, d.casalino@tudelft.nl, AIAA member.
‖Visiting Professor, Departamento de Bioingeniería e Ingeniería Aeroespacial, aianiro@ing.uc3m.es, AIAA member.

open questions which even challenge the quadrupole or dipole modeling of the phenomenon [1]. Most of the presented experimental analyses typically combine the temporal information from hot-wire anemometry (HWA) or microphones in the near or far field, with the availability of multi-point measurements such as particle image velocimetry (PIV).

Jung et al. [7] obtained for example a low-dimensional time-dependent reconstruction of the stream-wise velocity using the dominant modes reconstructed by proper orthogonal decomposition. In their setup, the authors scanned the first 6 diameters of a turbulent incompressible jet at high Reynolds number with a polar array of 138 synchronized straight hot-wire probes. In a later study, Iqbal and Thomas [8] used a particular implementation of the POD analysis to retrieve a helical vortex structure beyond the tip of the potential core of their jet. With stereo PIV and microphone measurements, Alkislar et al. [9] studied the effect of stream-wise vortices on axisymmetric micro-jets with chevrons. The use of tomographic PIV (Violato and Scarano [10]) has effectively demonstrated that the technique is able to relate the instantaneous turbulent structures with the activity of the acoustic sources. However, due to the limitations of conventional high-repetition PIV setups, a compromise between illuminated volume, speed of the jet or fluid density (water for larger seeding particles) and spatial resolution needs to be carried out. In particular, due to the acquisition limitations in the PIV hardware, complex setups have to be carried out whenever relatively high acquisition fre quencies have to be ensured for a correct representation of the flow field (i.e. > 20kHz). In the present paper the new technique based upon the work of Schneiders et al. [11] is applied to a circular jet at three different turbulent Reynolds numbers to retrieve both the time evolution of the velocity and of the fluctuating pressure. The particular technique allows for exploiting the relatively higher dynamic range and volumetric data density of low-repetition tomographic PIV setups to obtain the full evolution of the instantaneous 3D vector fields in time. Due to the finite marching of the vector field accomplished by the technique, a beneficial effect is expected when the fully developed jet is used for integration of the noise sources and propagation in the far field.

II. Experimental setup

An experimental setup is created for the study of a circular jet at different Reynolds number. In the full experimental campaign three nozzles respectively with a square, triangular and circular jet exit (Figure 1a) were installed in a dedicated settling chamber where a mixture of DEHS fluid diluted with air was pressurized to reach exit Reynolds-numbers between 5,000 and 20,000. The data pertaining to this manuscript focus on a circular configuration with Mach number below 0.1. The choice was made in order to both prove the technique as well as having a direct flow comparison with the results obtained from a similar jet with a tomographic-PIV high-repetition system (already available in literature [10]). Therefore, two PIV setups were prepared, a double stereoscopic PIV setup for validation of the jet mean-flow in the middle plane and a Tomographic PIV one, for the three-dimensional flow analysis, i.e. the development of the technique based upon the VIC methodology [11]. The two stereoscopic PIV setups, sketched in Fig. 1 were obtained by installing 4 LaVision ProLX cameras (4872x3248 MPix, 12 bit) at about 90 degrees angle in the azimuthal plane of the cylinder. Illumination is provided by a Spectra Physics Quanta Ray Nd:Yag laser with 400 mJ per pulse energy. The light is conveyed by laser optics to form a laser sheet of about 1 mm thickness. Four Nikon lenses with 200 mm focal length at $f_{\#} = 8$ are adopted together with 4 Scheimpflug adaptors to obtain two consecutive planar field of views of about 81 mm each combined into a single field of 153 mm (34 jet diameters). A total amount of 2000 uncorrelated image-pairs have been acquired at an acquisition frequency of about 1 Hz. The recordings are evaluated with the LaVision Davis 8.4 software, featuring a window-deformation iterative multi-grid [12] with window-size of 48 × 48 pixels at 75% overlap (vector spacing of 4.3 vectors per mm). Additionally, together with the stereoscopic setup a hot-wire anemometry setup was prepared to allow for a modal decomposition of the planar fields with respect to a time-resolved signal. Results of the HWA are not presented in the present manuscript. The tomographic PIV setup features instead the same 4 cameras in a new configuration at the four vertices of a paralleliped with 90 deg angle in the azimuthal plane of the nozzle and 45 deg angle in the vertical (stream-wise) direction. The particular setup allows investigating approximately 12 diameters of jet evolution, downstream of the nozzle exit plane, ideal for the computation of the pressure fluctuations along the jet axis. The illumination from the double-cavity Nd:Yag Spectra-Physics Quanta Ray PIV-400 laser was expanded to form a slowly-diverging conical volume able to both ensure enough particle scattering and low reflections from the jet exit. The tomographical reconstruction of the single snapshots into a volumes of particles is obtained by use of a Fast Multiplicative Algorithm for Tomographic Reconstruction in Davis 8.4 [13]. A volume of data of approximately 18 x 9 x 55 mm^3 with a digital resolution of 62 vxl/mm is generated, subsequently processed with a Fast Fourier Transform algorithm [14] with window size of 48 × 48 × 64 voxels and interpolated into a uniform grid with a vector spacing of 5.2 vectors per mm in the three directions. Following the procedure exposed in the work of Violato et al. [15], the uncertainty of the velocity is estimated to be 2% at the exit of the nozzle.

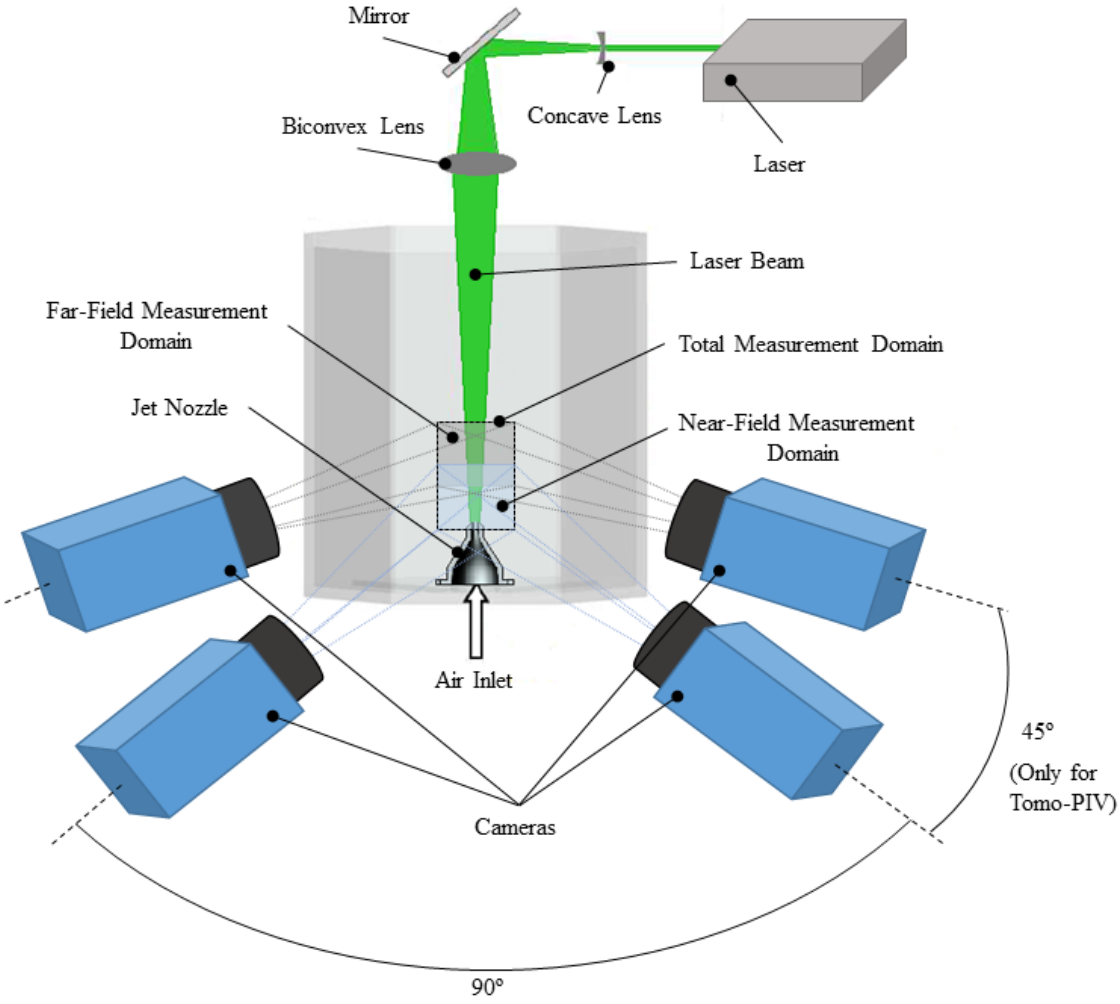

Fig. 1 Schematic of the double-stereoscopic PIV set-up.

III. Data processing

A. Vortex-In-Cell methodology

In the present study, the VIC technique, as detailed in Schneiders et al. [11], is employed to generate consecutive velocity fields from a finite marching of the actual measurements in 3D. The data as processed from the direct correlation technique are further filtered by an universal outliers-detection algorithm [16], to eliminate any vector resulting from loss of correlation due to non-uniformities in the particle distribution. An additional pre-step is carried out by imposing a divergence-free condition in the tomographic velocity field. Finite volumes around the experimental grid points are additionally generated. In the new grid, the new positions of the particles in time are calculated by means of a particle *advection* model [17]. The particle strength is computed with the *vortex stretching* model [18], and consecutively the vorticity at the grid nodes. A final step is carried out to calculate the new velocity fields by solving a Poisson equation with the advected vorticity in input and Neumann boundary conditions with null-gradient in the far field. A more detailed explanation of the approach and implementation is given in the work of Schneiders et al. [11]. The particular approach offers several foreseen advantages when studying jets flows. First, a full time sequence of velocity fields can be obtained from a single snapshot, provided that the advection model is able to accurately represent the flow physics and that the flow field offers sufficient spatial resolution to accurately describe the investigated flow structures. An

important advantage is related to the current limitations of high-speed cameras, which need a consistent lowering of the spatial resolution (< 2 MPix) to reach acquisition frequencies higher than 5 kHz [19].

B. Pressure Field Computation

In order to compute the pressure fluctuations in the jet volume, the Lagrangian material-derivative is calculated in time at fixed points in space by fitting the temporal variation of the velocity fields with a second order polynomial [20]. Two important assumptions are considered in this approach. First, the approach is expected to capture the velocity of the same particle in the neighborhood of the spatial point where the derivative is computed. This requirement would be fulfilled with a Δt between consecutive frames sufficiently small,

$$\Delta t \leqslant \frac{\Delta x}{U \cdot N_t} \tag{1}$$

where Δx is the grid spacing, U is the velocity magnitude at the point and N_t is the number of time frames employed for the fit. Second, the velocity variation in time in the stencil used for the Lagrangian evaluation of the derivatives is assumed to be small enough to be represented by a second-order polynomial. The flow pressure is obtained by means of a Poisson solver that integrates the pressure gradient computed from the Navier-Stokes momentum equation using the PIV velocity fields as input [21]. In particular, when considering a stationary orthonormal Cartesian frame of axis and the respective velocity vector $\vec{v}$, the pressure gradient reads:

$$\nabla p = -\rho \left(\frac{D\vec{v}}{Dt} \right) + \mu \nabla^2 \vec{v} = -\rho \left(\frac{\partial \vec{v}}{\partial t} + \vec{v} \cdot \nabla \vec{v} \right) + \mu \nabla^2 \vec{v} \tag{2}$$

where p, ρ and μ are respectively the flow pressure, density and dynamic viscosity, and the ∂ and D operators represent the partial and material (or total) flow derivatives. In the present study, the material derivative of the velocity is estimated using a least-squares fit of the velocities along a reconstructed particle trajectory in a similar way as in Pröbsting et al. [22]. The main changes with respect to the latter implementation is the employment of a stencil with n = 2 (i.e. 5 vector fields) and m = 2 (i.e. 2^{nd} order approximation of the flow curvature), which has been found to give already converged results for the time spectra. Boundary conditions are set by computing the normal components of the pressure gradient and used as Neumann boundary conditions in the stream-wise evolution of the jet. Dirichlet type boundary conditions are applied in the jet far-field.

IV. Validation

The stereoscopic PIV data are used for the validation of the jet experiment and statistics. In the following paragraph, statistics including mean flow velocity components and fluctuations are presented. A POD [23] decomposition is additionally carried out to visualize the most important aerodynamic modes for the jet evolution, the pairing phenomenon and the break-down of the flow structures.

A. 2D statistics

Results from the double stereo PIV configuration are combined to form a large region of interest as shown in Fig. 2. The velocities are non-dimensionalized with the axial velocity at the exit of the nozzle U_{max}. The near-region plane covers up to $z/D = 18$ with an overlap between the two combined fields of about 3 diameters distance. Mean-flow velocity components are presented on the left columns, while fluctuations are on the right. Velocity components are ordered in stream-wise v_z, radial v_r and azimuthal v_θ components normalized by the free-stream jet-exit velocity and arranged for clarity in an axisymmetric configuration with the flow from the left to the right. The potential jet-core with a stream-wise velocity component v_z/U_{max} larger than 0.9 is identified until about $z/D = 2.5$. A jet divergence angle of 10° from its own axis is additionally measured from the results. As mentioned in Section II, the presence of the hot-wire anemometer is seen at $z/D \approx 8$. As can be seen from the the mean radial flow component, a negligible contribution is appreciated in comparison to the azimuthal one, of about 7% of the original stream-wise component. Fluctuations of about 2% are appreciated in the inner jet core, which raise up to about 20% in the shear-layer region. At about 10 diameters, the flow fluctuations start rapidly decaying down to about 1%. The stream-wise components of the velocity profiles are extracted at the center of the jet and normalized with the free-stream speed in Fig. 3. The region affected by the hot-wire anemometer $7 < x/D < 9$ was carefully interpolated retrieving the underlying trend.

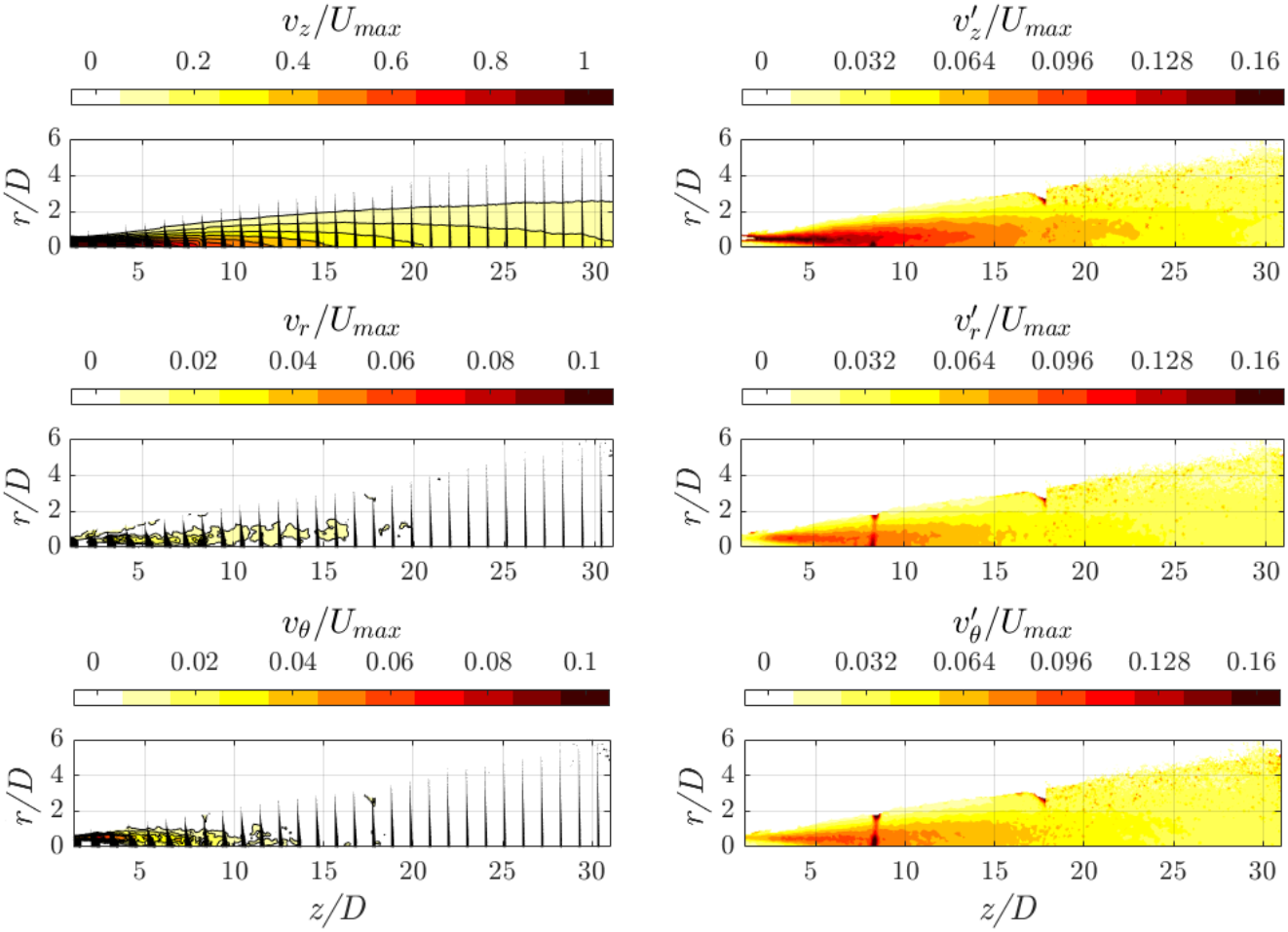

Fig. 2 Mean cylindrical velocity components (left) and fluctuating velocity components (right) for the axisymmetric jet at $Re = 5000$**.**

Downstream of this region, the velocity decays until reaching v_z/U_{max} at the farthest axial distance from the nozzle, $z/D = 30$. The turbulent kinetic energy (*tke*) for the case of $Re = 10000$ exhibits unnatural behavior below $x/D = 3$, with a local peak of energy at the exit of the nozzle. The most probable reason for this crest is the lack of correct vectors in the region close to the nozzle due to its reflections, and so the loss of information when averaging in time.

Fig. 4 presents the same extrapolations for the three velocity components in terms of fluctuations along the centerline. As seen in the original contours of Fig. 2 the fluctuations of the axial component of the velocity are the most important ones, in a range between 5 and 13% of the stream-wise exit velocity for all configurations. In particular, it is appreciated that the highest Reynolds case exhibits a higher discrepancy with the two other cases for the azimuthal component than for the axial and radial ones, for which the difference between the cases is lower than 1%. From the exit of the nozzle the velocity fluctuations increase until reaching a peak around $z/D \approx 7$ independently of the configuration, from which they homogeneously decay downstream throughout the mixing region. This peak of RMS and turbulent kinetic energy may coincide with the end of the potential core [24].

V. VIC-BASED 3D JET EVOLUTION

A 3D analysis is performed by applying the Vortex-In-Cell [11] technique to the vector fields obtained with tomographic PIV. Special care must be taken when applying the approach to jet data, as a sufficient long time of

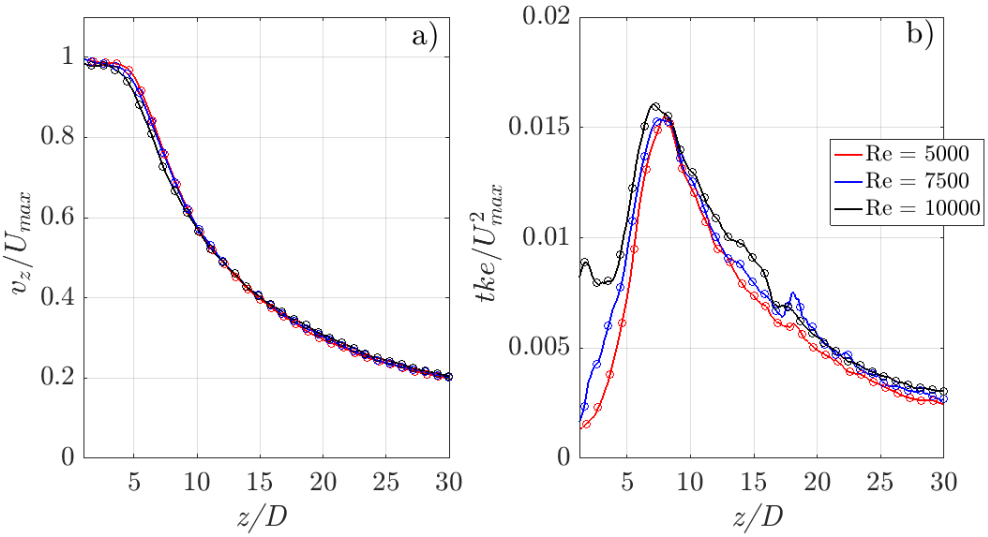

Fig. 3 a) Stream-wise velocity and b) turbulence kinetic energy for the centerline of the jet at the Reynolds 5000, 7500 and 10000.

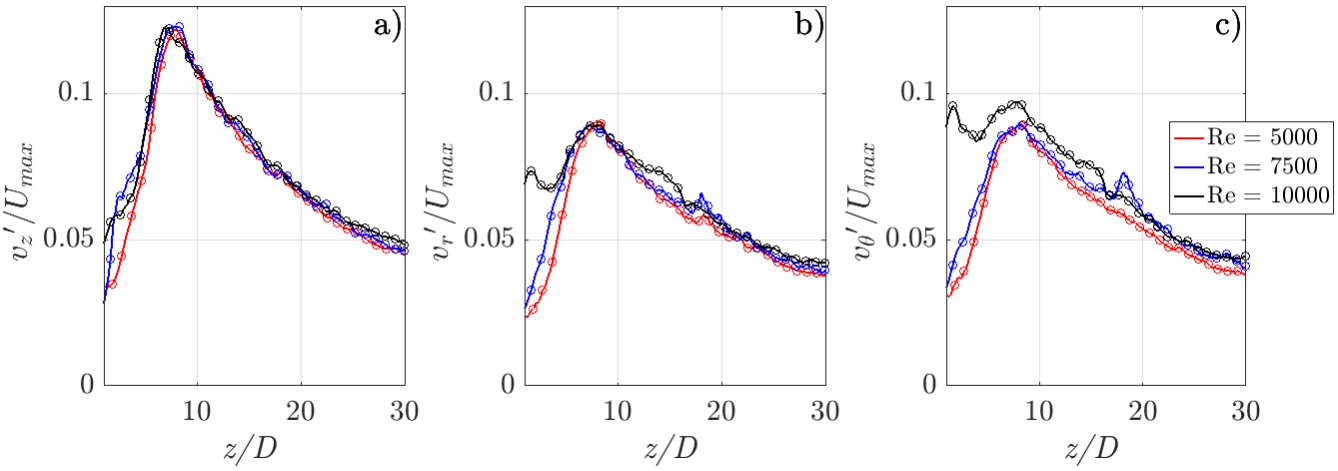

Fig. 4 Velocity RMS of the three components: a) axial, b) radial and c) tangential for the Reynolds 5000, 7500 and 10000.

propagation would lead to a divergent instability far away from the physical coherence. This propagation time limit determines the lowest frequency captured by the spectrum, so it is of critical importance to achieve the longest propagation time possible in order to obtain a spectrum with a sufficiently large frequency range. In the present case, it was achieved a total time of 1 ms that corresponds to a lower limit for the frequency range of $f = 1$ kHz.

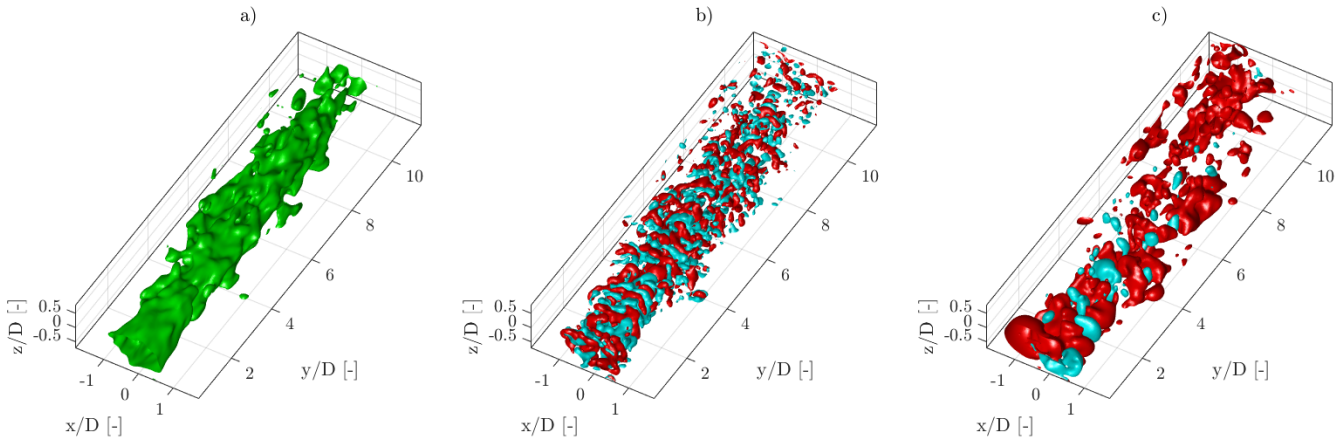

Fig. 5 Instantaneous 3D flow field: a) velocity magnitude with $V/U_{max} = 0.3$ in green, b) Q-criterion with $Q \cdot D^2/U_{max}^2 = 0.05$ in cyan and $Q \cdot D^2/U_{max}^2 = -0.05$ in red, c) integrated pressure with $\Delta p/\rho_\infty U_{max}^2 = 0.01$ in red and $\Delta p/\rho_\infty U_{max}^2 = -0.01$ in cyan.

A single tomographic vector-field used for the computations are shown in Fig. 5, which entails an effective axial distance of 12 diameters. Velocity magnitudes and contours of Q are presented in Fig. 5 too. The contour of velocity magnitude $U/U_{max} = 0.3$ clearly shows the turbulent nature of the jet past $x/D \approx 2$, from which the high-speed region breaks down into smaller scales, the size of which slowly keep decreasing as convecting downstream. The same behavior is appreciated with the corresponding Q-criterion visualization, with similar flow scales. Moreover, alternating positive and negative vortical regions are appreciated throughout the length of the jet indicating the presence of a series of low and high pressure fluctuations moving downstream. The alternating region of high and low vortex deformation are well-documented in literature as corresponding to Kelvin–Helmholtz roll-up instabilities, producing 3D ring-like shapes as also visualized by Violato [10]. The pressure fluctuations follow the evolution of the instabilities with regions of high and low pressure with about 5 Pa variation in the full domain. The actual increase of positive pressure fluctuations from $x/D = 4$ is indicative of the overall decelerating flow along the stream-wise direction.

A. 3D evolution of the jet

The evolution of the artificial jet field created by the VIC finite marching is presented, as well as the associated second invariant of the velocity field, in Fig. 6. The time separation between two consecutive given frames of the shown evolution is $dt = 1.5 \cdot 10^{-4} s$ corresponding to a frequency of 6,666.7 Hz. Results show oscillations developing on the velocity iso-contours from time t_4, Fig. 6(d), around the location $y/D = 2$. These seem to trigger local instability to the breakdown of the Q-contours observed along the jet development. The effect of the propagation on the Q-criterion is indicated by the diffusion of the rounded-lobed structures, shown in Fig. 6(a), stretching until reaching the elongated filament structures displayed in Fig. 6(e).

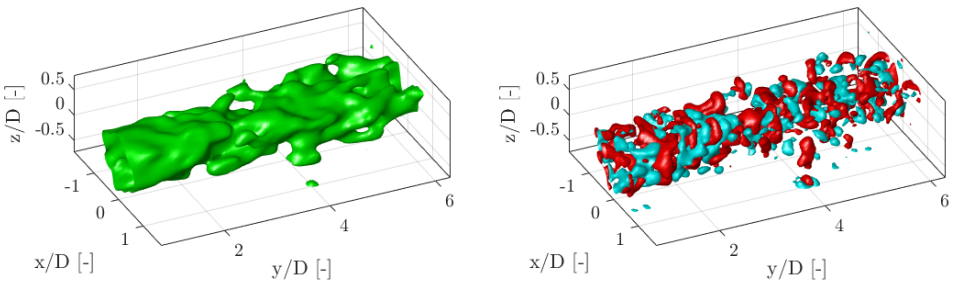

(a) Time t_1

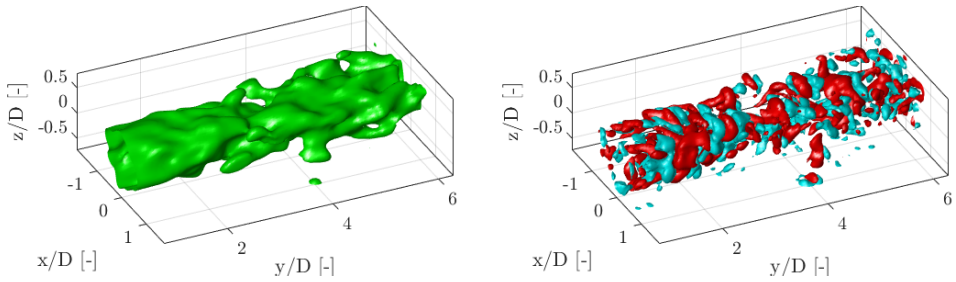

(b) Time t_2

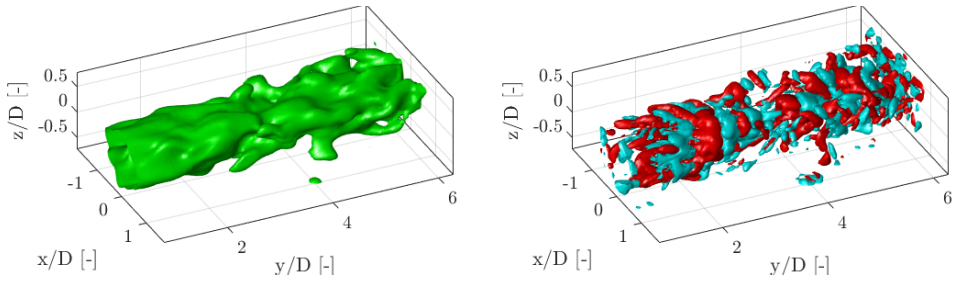

(c) Time t_3

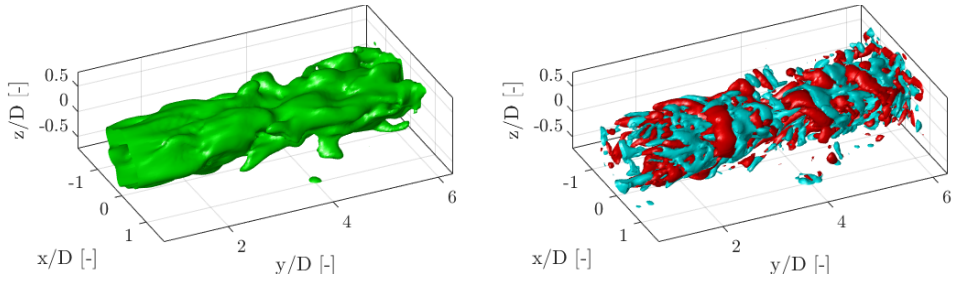

(d) Time t_4

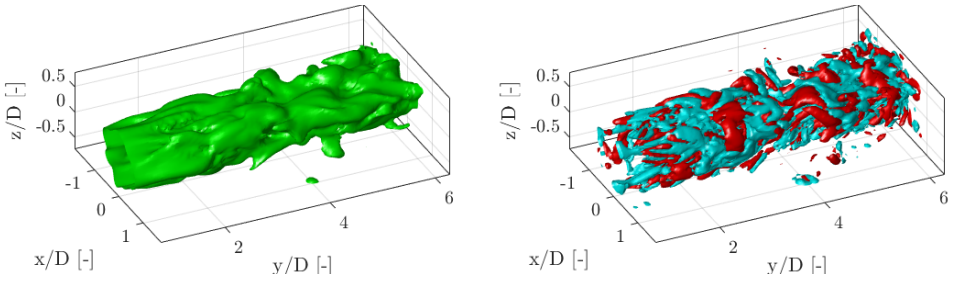

(e) Time t_5

Fig. 6 Time sequence visualization of the jet velocity (left) and Q (right) for the circular jet. Iso-surfaces of velocity magnitude $V/U_{max} = 0.3$ (green), and Q-criterion $Q \cdot D^2/U_{max}^2 = 0.05$ (cyan) and $Q \cdot D^2/U_{max}^2 = -0.05$ (red). Time separation between displayed images $\Delta t = 1.5 \times 10^{-4} s$.

VI. 3D pressure field

The following section aims at showing that the resulting pressure field, and consequently the spectra of the pressure fluctuations, can be obtained from a single-snapshot approach.

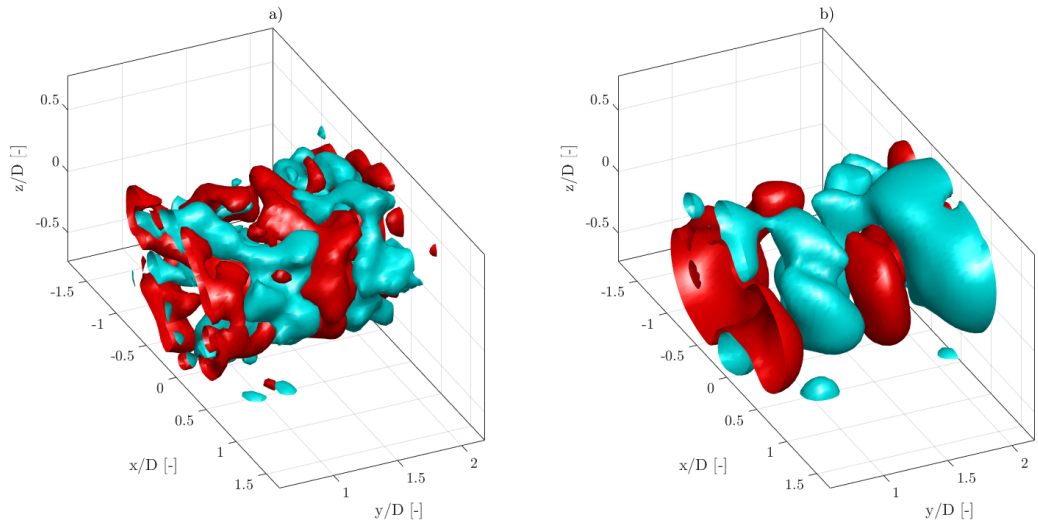

Fig. 7 Visualization of a) Q-criterion and b) pressure fluctuations for the range $0.5 < y/D < 2$. Iso-surfaces of Q-criterion, with $Q \cdot D^2/U_{max}^2 = 0.05$ in cyan and $Q \cdot D^2/U_{max}^2 = -0.05$ in red, and pressure fluctuations, with $\Delta p/\rho_\infty U_{max}^2 = 0.01$ in red and $\Delta p/\rho_\infty U_{max}^2 = -0.01$ in cyan.

Figure 7 depicts Q-and pressure fluctuations contours in a range between $0.5D$ to $2D$, with red and cyan surfaces for positive and negative Q and vice-versa for the pressure. Both results agree in showing a similar topology of the highly vortical structures with the low pressure regions. In particular, four regions in the axial direction with alternating sign recall the distribution of the azimuthally distributed vorticity structures caused by Kelvin–Helmholtz roll-up instabilities. For axial distances longer than $x/D = 2$, the pairing process of two consecutive structures de-correlates the pressure fluctuations with respect to the Q contours. In addition, it can be noted that the length-scales of the pressure fluctuations is about double the one of the associated Q structures, as reported by [25]. In the reminder of the document the extraction of the pressure fluctuations is carried out and compared to results present in literature.

A. Jet spectra

The characterization of the spectral content of the velocity and pressure fluctuations is carried out here by means of a conventional Welch technique [26] based on a fast Fourier analysis with blocks of 1024 images and an overlap of 50%. A single sequence of 2000 snapshots generated by the VIC methodology separated by a $\Delta t = 5 \times 10^{-7}$ seconds corresponding to a marching frequency of $f_m = 2 \times 10^6$ Hz is used for the computation of the spectra. In order to reduce the uncertainty on the single pressure signal, the pressure spectra were averaged along a circumference centered at the jet axis. A second assumption relies on the directivity of the jet being axisymmetric.

The time series pertaining to all points used for the computations of the spectra are given as pressure and velocity fluctuations in Fig. 8. The velocity fluctuations are given in the Cartesian reference frame for an easier comparison with literature. The axial velocity presents the strongest fluctuations, $v_y'/U_{max} = 0.4$, while the span-wise and vertical components show the same mean amplitude. The pressure variations oscillate between $0.02 < \Delta p/\rho_\infty U_{max}^2 < -0.02$.

Spectra of both pressure and velocity fluctuations, non-dimensionless with $\left(\frac{1}{2}\rho_0 U_{max}^2\right)^2$ and U_{max}^2 in Fig. 9(a) and Fig. 9(b) respectively, exhibit a low-frequency over-prediction followed by a logarithmic decay in the high-frequency range. It is shown the trend of the experimental results of Power et al. [27] as a black dashed line in Fig. 9(a) as reference. The similarity between the curves for $St > 1$ is fair, both following the same energy dissipation behavior for high frequencies. Below $St = 1$, the pressure spectra tend to flatten, recalling the far field spectra at low frequencies [28]; however, the dynamic range of the current volume might not be enough at low Strouhal numbers to capture the lowest frequency components. In Fig. 9(b) the trend from experimental data from Grizzi and Camussi [29] for near-field pressure fluctuations is added, revealing a f^{-2} slope. There is very good agreement between the slopes of the present signal and the reference one for $St > 1$, proving the validity of the exposed methodology. A higher discrepancy is found

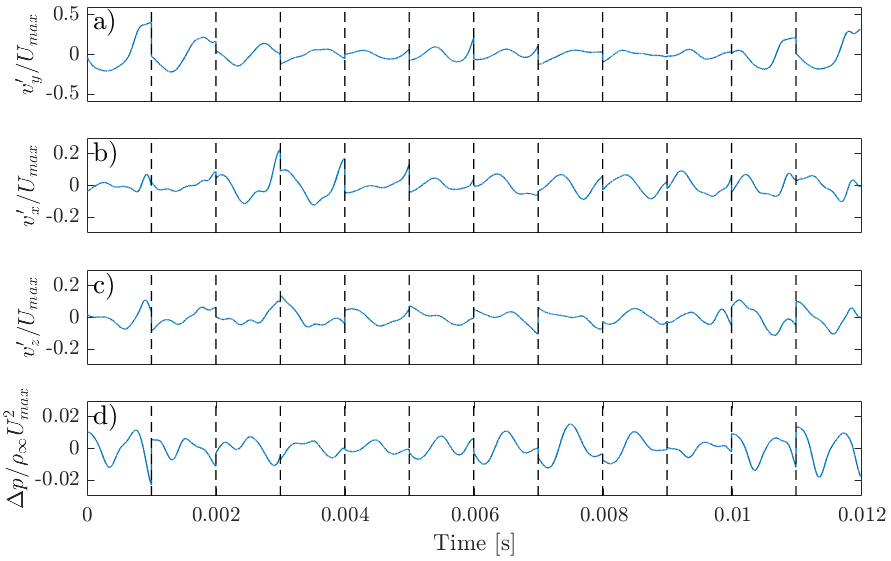

Fig. 8 Time-series of velocity fluctuations(a) axial, b) span-wise and c) vertical) and d) pressure fluctuations for an azimuthal ring with $r/D = 1$ at $x/D = 2.5$.

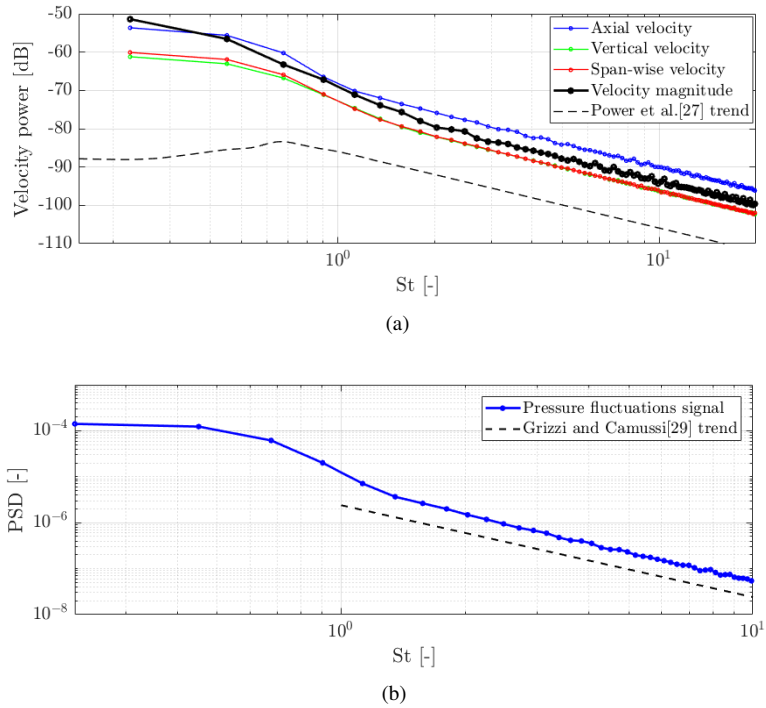

Fig. 9 Velocity fluctuations spectra (a) and pressure fluctuations spectra (b) for an azimuthal ring with $r/D = 1$ at $x/D = 2.5$.

for lower frequencies but yet expected due to the lower dynamic range.

VII. Conclusion

A computational analysis of the VIC methodology applied to jet flows has been carried out to prove the validity of the method in extracting pressure fluctuations from a single tomographic PIV image. The methodology offers an alternative way to study the 3D evolution of the flow field in absence of a high-repetition PIV system.

The technique has first been applied to the study of a circular jet flow evolution at low Reynolds and Mach number. Provided that a sufficiently large volume and spatial-dynamic range is given, the technique is able to retrieve velocity and pressure in time, as well as pressure spectra, from which it can be extracted noise estimations by the application of an acoustic analogy.

Derivation from the experimental velocity field of the 3D pressure fluctuations showed a close agreement between the flow structures as visualized by the Q-criterion and the alternating positive and negative pressure fluctuations in the flow field. Pressure spectra were additionally obtained from a single snapshot of 3D tomographic PIV. Although the frequency range is limited by the volume size and by the actual spatial resolution of the flow field (entailing the minimum Δt that can be used in the marching), the turbulence and pressure decay trend reflects the values reported in literature. At the low frequency range, the achieved spectrum from the set of VIC fields illustrated a flat trend typical of far field sound pressure spectra [28]. Nevertheless, the decaying behavior did match the slope reported by the references [27] [29], for the turbulence and pressure respectively, indicating an agreement on the energy dissipation mechanism.

Future work is dedicated to obtain a forward and backward finite marching of the field to generate a longer time sequence for the integration of the pressure fluctuations in sound pressure level. The Lighthill's noise analogy is being implemented and applied to the shown data to compute the far field spectrum. Additionally, further analyses are done on square and triangular geometries, in order to study the singular 3D behavior of the flow emerging from these exits.

References

[1] Suzuki, T., "A review of diagnostic studies on jet-noise sources and generation mechanisms of subsonically convecting jets," *Fluid Dynamics Research*, Vol. 42, No. 1, 2010, p. 014001.

[2] Fu, Z., Agarwal, A., Cavalieri, A. V., Jordan, P., and Brès, G. A., "Turbulent jet noise in the absence of coherent structures," *Physical Review Fluids*, Vol. 2, No. 6, 2017, p. 064601.

[3] Mollo-Christensen, E., "Jet noise and shear flow instability seen from an experimenter's viewpoint," *Journal of Applied Mechanics*, Vol. 34, No. 1, 1967, pp. 1–7.

[4] Crow, S. C., and Champagne, F., "Orderly structure in jet turbulence," *Journal of Fluid Mechanics*, Vol. 48, No. 3, 1971, pp. 547–591.

[5] Mankbadi, R., and Liu, J., "Sound generated aerodynamically revisited: large-scale structures in a turbulent jet as a source of sound," *Phil. Trans. R. Soc. Lond. A*, Vol. 311, No. 1516, 1984, pp. 183–217.

[6] Cavalieri, A. V., Jordan, P., Colonius, T., and Gervais, Y., "Axisymmetric superdirectivity in subsonic jets," *Journal of fluid Mechanics*, Vol. 704, 2012, pp. 388–420.

[7] Jung, D., Gamard, S., and George, W. K., "Downstream evolution of the most energetic modes in a turbulent axisymmetric jet at high Reynolds number. Part 1. The near-field region," *Journal of Fluid Mechanics*, Vol. 514, 2004, pp. 173–204.

[8] Iqbal, M., and Thomas, F., "Coherent structure in a turbulent jet via a vector implementation of the proper orthogonal decomposition," *Journal of Fluid Mechanics*, Vol. 571, 2007, pp. 281–326.

[9] Alkislar, M. B., Krothapalli, A., and Butler, G., "The effect of streamwise vortices on the aeroacoustics of a Mach 0.9 jet," *Journal of Fluid Mechanics*, Vol. 578, 2007, pp. 139–169.

[10] Violato, D., and Scarano, F., "Three-dimensional vortex analysis and aeroacoustic source characterization of jet core breakdown," *Physics of fluids*, Vol. 25, No. 1, 2013, p. 015112.

[11] Schneiders, J. F., Dwight, R. P., and Scarano, F., "Time-supersampling of 3D-PIV measurements with vortex-in-cell simulation," *Experiments in Fluids*, Vol. 55, No. 3, 2014, p. 1692.

[12] Scarano, F., and Riethmuller, M. L., "Iterative multigrid approach in PIV image processing with discrete window offset," *Experiments in Fluids*, Vol. 26, No. 6, 1999, pp. 513–523.

[13] Gordon, R., Bender, R., and Herman, G. T., "Algebraic reconstruction techniques (ART) for three-dimensional electron microscopy and X-ray photography," *Journal of theoretical Biology*, Vol. 29, No. 3, 1970, pp. 471–481.

[14] Elsinga, G. E., Scarano, F., Wieneke, B., and van Oudheusden, B. W., "Tomographic particle image velocimetry," *Experiments in fluids*, Vol. 41, No. 6, 2006, pp. 933–947.

[15] Violato, D., and Scarano, F., "Three-dimensional evolution of flow structures in transitional circular and chevron jets," *Physics of Fluids*, Vol. 23, No. 12, 2011, p. 124104.

[16] Westerweel, J., "Efficient detection of spurious vectors in particle image velocimetry data," *Experiments in Fluids*, Vol. 16, No. 3-4, 1994, pp. 236–247.

[17] Scarano, F., and Moore, P., "An advection-based model to increase the temporal resolution of PIV time series," *Experiments in fluids*, Vol. 52, No. 4, 2012, pp. 919–933.

[18] Koumoutsakos, P., "Multiscale flow simulations using particles," *Annu. Rev. Fluid Mech.*, Vol. 37, 2005, pp. 457–487.

[19] Scarano, F., "Tomographic PIV: principles and practice," *Measurement Science and Technology*, Vol. 24, No. 1, 2012, p. 012001.

[20] Violato, D., Moore, P., and Scarano, F., "Lagrangian and Eulerian pressure field evaluation of rod-airfoil flow from time-resolved tomographic PIV," *Experiments in fluids*, Vol. 50, No. 4, 2011, pp. 1057–1070.

[21] Van Oudheusden, B., "PIV-based pressure measurement," *Measurement Science and Technology*, Vol. 24, No. 3, 2013, p. 032001.

[22] Pröbsting, S., Scarano, F., Bernardini, M., and Pirozzoli, S., "On the estimation of wall pressure coherence using time-resolved tomographic PIV," *Experiments in fluids*, Vol. 54, No. 7, 2013, p. 1567.

[23] Berkooz, G., Holmes, P., and Lumley, J. L., "The proper orthogonal decomposition in the analysis of turbulent flows," *Annual review of fluid mechanics*, Vol. 25, No. 1, 1993, pp. 539–575.

[24] Aleyasin, S. S., Tachie, M. F., and Koupriyanov, M., "PIV Measurements in the Near and Intermediate Field Regions of Jets Issuing From Eight Different Nozzle Geometries," *Flow, Turbulence and Combustion*, Vol. 99, No. 2, 2017, pp. 329–351.

[25] Ghaemi, S., Ragni, D., and Scarano, F., "PIV-based pressure fluctuations in the turbulent boundary layer," *Experiments in fluids*, Vol. 53, No. 6, 2012, pp. 1823–1840.

[26] Welch, P., "A fixed-point fast Fourier transform error analysis," *IEEE Transactions on Audio and Electroacoustics*, Vol. 17, No. 2, 1969, pp. 151–157.

[27] Power, O., Kerhervé, F., Fitzpatrick, J., and Jordan, P., "Measurements of turbulence statistics in high subsonic jets," *10th AIAA/CEAS Aeroacoustics Conference*, 2004, p. 3021.

[28] Laurence, J. C., "Intensity, scale, and spectra of turbulence in mixing region of free subsonic jet," 1956.

[29] Grizzi, S., and Camussi, R., "Wavelet analysis of near-field pressure fluctuations generated by a subsonic jet," *Journal of Fluid Mechanics*, Vol. 698, 2012, pp. 93–124.